FRONTIERS OF PHYSICS

RESEARCH ARTICLE
Volume 20 / Issue 6 / 064203 / 2025

Chiral metasurfaces enabling tunable spin selection for multidimensional images and beam splitting

Chengxin Cai[1], Yinfei Li[1,4], Yangyang Zhou[1,2,3,†], Quan Pan[5]

1 Key Laboratory of Grain Information Processing and Control (Henan University of Technology) of Ministry of Education, Zhengzhou 450001, China
2 Department of Physics, Shantou University, Shantou 515063, China
3 The Science and Technology on Reliability Physics and Application of Electronic Component Laboratory, Electronic Produce Reliability and Environmental Testing Research Institute, Guangzhou 510610, China
4 College of Communication and Information Engineering, Chongqing College of Mobile Communication, Chongqing 401400, China
5 School of Automation, Northwestern Polytechnical University, Xi'an 710072, China
Corresponding author. E-mail: †zhouyangyang0623@163.com
Received February 27, 2025; accepted May 13, 2025

© Higher Education Press 2025

ABSTRACT

Controlling the spin angular momentum or circular polarization state of waves has crucial applications in circular dichroism spectroscopy, optical communications, and information processing. Traditional chiral metasurfaces, however, have fixed electromagnetic responses and modulation functions post-fabrication, which significantly limits their practical applications. This limitation is particularly evident in their lack of active control and tunability, hindering further development of electromagnetic functional devices. In this work, we propose a Metal–Insulator–Metal (MIM) chiral metasurface (CM) achieve multidimensional control of light based on amplitude modulation along with frequency and temperature adjustments in polarization multiplexing. Based on the design metasurface, we obtain the multi-dimensional switchable images and integrated beam splitter with varying polarization conversion properties. Additionally, a tunable anomalous reflection function also is constructed by leveraging the phase transition characteristics of vanadium dioxide. The multi-dimensionally controllable and multifunctional chiral metasurface introduces new functionalities, offering promising prospects for the design of future integrated functional devices.

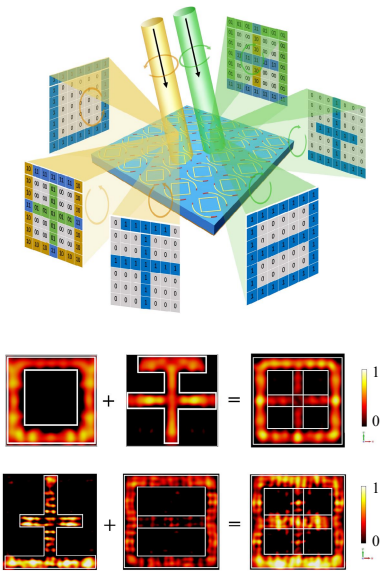

Keywords chiral metasurface, amplitude, beam splitter, multi-dimensional switchable images, vanadium dioxide

1 Introduction

Metasurfaces, as defined in the literature [1, 2], are two-dimensional artificial structures consisting of a periodic array of subwavelength units made of metal or dielectric materials. These structures offer extensive degrees of freedom to manipulate the phase [3–5], amplitude [6, 7], and polarization [8–13] of light using subwavelength geometries. Compared to traditional optical devices,

*Special Topic: Advances in Metamaterials: Harnessing the Power of Spatial and Time Assembly (Eds.: Minghui Lu, Huanyang Chen & Xiujuan Zhang).

Higher Education Press

https://doi.org/10.15302/frontphys.2025.064203

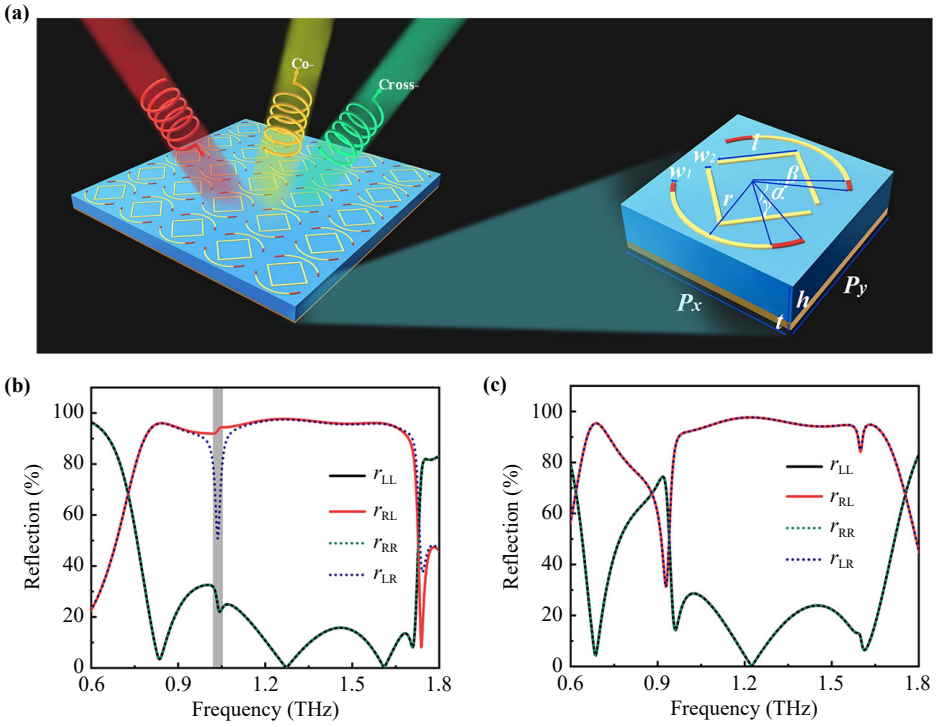

Fig. 1 **(a)** Schematic diagram of the designed chiral metasurface. The reflection coefficients for **(b)** the dielectric state and **(c)** the metallic state of VO_2.

metasurfaces provide significant advantages due to their ultrathin profile, high efficiency, and broadband capabilities. Consequently, they have enabled a range of applications including anomalous refraction [14–16], vortex beam generation [17–21], holographic imaging [22–25], bessel beams [26], and metalenses [27–32]. Beyond single functionalities, metasurfaces have facilitated advanced multiplexing capabilities in wavelength [33–38], angle [39–42], and orbital angular momentum (OAM) [43, 44], as well as the development of reconfigurable metadevices [45, 46].

Polarization, a key property of light, has been extensively utilized in metasurfaces for high-capacity multiplexing technologies, enabling the transmission of information across independent channels to specified targets. Recent advancements have expanded polarization multiplexing from two channels [47] to multiple channels [48, 49] within a single-layer metasurface. Specifically, polarization multiplexing metasurfaces, particularly those employing chiral superstructures for circular polarization, have emerged as platforms for exploring novel physics and applications. To further enhance metasurface applications, amplitude modulation has been integrated into polarization multiplexing, leading to the simultaneous design of devices capable of nano-printing and holography in the near- and far-field, respectively. By incorporating multidimensional multiplexing of wavelength, amplitude, and polarization, metasurfaces now offer comprehensive functionalities, including multidimensional imaging [50, 51] and advanced holography [52–60].

In this work, we introduce amplitude modulation along with frequency and temperature adjustments in polarization multiplexing to propose a Metal–Insulator–Metal (MIM) chiral metasurface (CM) featuring double split-ring resonators. This design aims to achieve multidimensional control of light, leveraging the broadband chiral responses and geometric phase modulation within the terahertz spectrum. By varying geometric parameters, CMs with distinct circular polarization conversion efficiencies are produced. Additionally, the integration of vanadium dioxide (VO_2) enables tunable chiral light responses. Building on these capabilities, we demonstrate a multiplexed, switchable imaging system controlled by incident wavelength and reflection polarization. Moreover, by incorporating geometric phase control into the CMs, we design a tunable-focus metalens capable of selective spin focusing and other diverse functions. Furthermore, we design a tunable polarization multiplexed broadband circular beam splitter. This integrated metasurface thus offers unprecedented control over both input and output optical parameters, paving the way for novel functionalities at the microscale.

2 Theorical analysis and device design

The geometric parameters of the multifunctional chiral metasurface are depicted in Fig. 1(a), which consists of

double split-ring resonators made of Au and VO_2, a dielectric layer of polyester film (Mylar), and a gold reflective substrate, all arranged periodically. The dimensions of the metasurface unit cell in the x and y directions are $P_x = P_y = 120$ μm, while the thicknesses of the dielectric layer (Mylar) and the metal layer (Au) are $h = 30$ μm and $t = 0.2$ μm, respectively. Concerning the design of the resonant structures, the radius and width of the circular double split-ring resonators are $r = 56$ μm and $w_1 = 3$ μm, respectively. Similarly, the arm length and width of the rectangular double split-ring resonators are $l = 56$ μm and $w_2 = 3$ μm, respectively, with a separation of $y_1 = 50$ μm between the upper and lower components. Before synthesizing the arcs of the circular double split-ring resonators, a ring with $r = 56$ μm and $w_1 = 3$ μm was first synthesized on the upper layer of the metasurface. It was then symmetrically cut at an angle of $\alpha = 60°$, and the vanadium dioxide structure was introduced through asymmetric cuts at angles of $\gamma = 10°$ and $\beta = 20°$.

In this work, the unit structure of the designed multifunctional chiral metasurface exhibits a unique working mechanism, which mainly stems from its special structural design and the properties of the selected materials. Gold has good electrical conductivity and stable chemical properties [61], and Mylar has excellent mechanical properties and can provide stable structural support [62]. Therefore, this metasurface is composed of a double open-loop resonator formed by gold (Au) and vanadium dioxide (VO_2), a dielectric layer of polyester film (Mylar), and a reflective substrate made of gold, all of which are arranged periodically. In terms of structure, the geometric parameters of the double open-loop resonator play a crucial role in its electromagnetic response. These include the radius and width of the circular double open-loop resonator, the arm length and width of the rectangular double open-loop resonator, as well as the spacing between the upper and lower components. These specific dimensions determine the response characteristics of the resonator to electromagnetic waves of different frequencies, enabling the metasurface to effectively manipulate light in specific frequency bands.

Furthermore, we incorporated the phase change material vanadium dioxide asymmetrically on both sides of the arcs of the circular double split-ring resonators to enable active control of the metasurface. In this structural configuration, we considered two specific states of the phase change material vanadium dioxide. At room temperature (prior to the phase transition), the material is in an insulating state, characterized by a dielectric constant of $\varepsilon_\iota = 9$ and a conductivity of $\sigma = 200$ S/m [48]. This means that in this state, vanadium dioxide has a relatively weak response to the electric field. The movement of electrons inside it is highly restricted, making it difficult to form an effective current conduction path, thus exhibiting insulating properties. The existence of this insulating state gives the metasurface specific electromagnetic characteristics at 1.034 THz. For example, at 1.034 THz, it has a high scattering ability to the r_{LR} wave, enabling preliminary control of electromagnetic waves. When it transitions to the metallic state (after the phase transition), its complex dielectric constant is described by the Drude model [49]. The Drude model is a classical model that describes the behavior of free electrons in metals. It regards the electrons in metals as a free electron gas. Under the action of an external electric field, the electrons will undergo collective oscillations. Therefore, when vanadium dioxide is in the metallic state, the internal electron freedom increases, and the electrons can move relatively freely in the material, resulting in good electrical conductivity. The real and imaginary parts of the complex dielectric constant reflect the material's ability to store and dissipate the electric field, respectively. In the metallic state, the real and imaginary parts of the complex dielectric constant of vanadium dioxide change significantly, leading to electromagnetic wave response characteristics that are completely different from those in the insulating state. When the temperature exceeds 68 °C, the material undergoes a phase transition from the dielectric state to the metallic state. This temperature-based phase transition characteristic provides an effective means for the active control of the metasurface. By controlling the temperature, we can flexibly adjust the state of vanadium dioxide, and thus achieve dynamic control of the electromagnetic characteristics of the metasurface.

For the analysis of the chiral metasurface unit, the Jones matrix is employed to examine the changes in the polarization state of electromagnetic waves. Within the Cartesian coordinate system, based on the theory of selective absorption and reflection of circularly polarized waves [50], the relationship between the incident and reflected electric fields of linearly polarized electromagnetic waves can be expressed as

$$\begin{pmatrix} \boldsymbol{E}_{\mathrm{r}}^{x} \\ \boldsymbol{E}_{\mathrm{r}}^{y} \end{pmatrix} = \begin{pmatrix} r_{xx} & r_{xy} \\ r_{yx} & r_{yy} \end{pmatrix} \begin{pmatrix} \boldsymbol{E}_{\mathrm{i}}^{x} \\ \boldsymbol{E}_{\mathrm{i}}^{y} \end{pmatrix} = R \begin{pmatrix} \boldsymbol{E}_{\mathrm{i}}^{x} \\ \boldsymbol{E}_{\mathrm{i}}^{y} \end{pmatrix}. \tag{1}$$

Here, $\boldsymbol{E}_{\mathrm{r}}$ and $\boldsymbol{E}_{\mathrm{i}}$ denote the reflected and incident electric fields, respectively; r represents the reflection coefficient, with subscripts x and y indicating the directions of linear polarization; $\boldsymbol{R}$ is the reflection matrix composed of these reflection coefficients. Through matrix transformation, the linearly polarized basis reflection matrix $\boldsymbol{R}$ can be converted into a circularly polarized basis reflection matrix $\boldsymbol{R}_{\mathrm{circ}}$:

$$\begin{aligned} \boldsymbol{R}_{\mathrm{circ}} &= \begin{pmatrix} r_{LR} & r_{LL} \\ r_{RR} & r_{RL} \end{pmatrix} = \Lambda^{-1}\mathrm{R}\Lambda \\ &= \frac{1}{2}\begin{pmatrix} r_{xx}+r_{yy}+\mathrm{i}(r_{xy}-r_{yx}) & r_{xx}-r_{yy}-\mathrm{i}(r_{xy}+r_{yx}) \\ r_{xx}-r_{yy}+\mathrm{i}(r_{xy}+r_{yx}) & r_{xx}+r_{yy}-\mathrm{i}(r_{xy}-r_{yx}) \end{pmatrix}. \end{aligned} \tag{2}$$

In this equation, the transformation matrix is denoted by $\Lambda = \frac{1}{\sqrt{2}} \begin{pmatrix} 1 & 1 \\ \mathrm{i} & -\mathrm{i} \end{pmatrix}$. The terms r_{LL} and r_{RR} refer to the co-polarization reflection coefficients of the unit, whereas r_{LR} and r_{RL} denote the cross-polarization reflection coefficients, with the subscripts "L" and "R" representing left-handed circular polarization (LCP) and right-handed circular polarization (RCP) waves, respectively, as viewed along the direction of the wave vector. By exploiting the differential optical responses of chiral enantiomers under the influence of LCP and RCP, this characteristic of chiral metasurfaces facilitates spin-selective multifunctional applications.

In the design of the MIM chiral metasurface, by designing a specific Jones matrix, the incident circularly polarized light can be converted into different types of circularly polarized light. When studying the modulation of terahertz waves by the chiral metasurface, the analysis using the Jones matrix reveals that when VO_2 is in the dielectric state, the chiral metasurface unit can achieve polarization conversion for the vertically incident LCP and RCP waves near 1.034 THz. This polarization conversion is precisely achieved through the characteristics of the Jones matrix of the interaction between the metasurface structure and light. Therefore, by designing an appropriate Jones matrix, the chiral metasurface can enhance or suppress the light of specific polarization components, and construct polarization-selective devices. To investigate the chiral response of chiral metasurfaces, we performed comprehensive full-wave numerical simulations to determine the reflection coefficients of the chiral unit structures when subjected to LCP and RCP waves incident perpendicular to the metasurface's normal, as illustrated in Fig. 1(a). This paper focuses on the behavior of VO_2 in both its dielectric and metallic states. In its dielectric state, the inherent asymmetry of the VO_2 layers facilitated the use of vertically incident LCP and RCP terahertz waves for excitation. Observations revealed that both LCP and RCP terahertz waves demonstrated broadband polarization conversion within the frequency range of 0.7 to 1.7 THz.

Numerical simulations are performed by using the frequency domain solver of the software CST Microwave Studio. Periodic boundary conditions are applied in the x and y directions to characterize the periodic structure, which can simulate the situation of an infinitely large periodic array. Open boundary conditions are set in the z direction to simulate the free space environment, thereby avoiding the interference of reflections on the simulation results. Moreover, an adaptive meshing technique is adopted. For the complex structure of the MIM CM, the meshing is refined near the double open-loop resonators in the key areas to obtain more accurate electromagnetic changes and improve the simulation accuracy. At the same time, the maximum and minimum values of the global mesh size are set to ensure a balance between the overall calculation accuracy and calculation efficiency. A terahertz wave with TM polarization is selected as the incident wave. The frequency scanning range is set to 0–2.0 THz, and the step size is set to 0.01 THz. This step size can not only ensure sufficient frequency resolution to accurately capture the variation trend of the reflection coefficient with frequency, but also avoid excessive computational complexity. Within this frequency range, the reflection coefficient corresponding to each frequency point is recorded in detail, thus drawing the accurate reflection coefficient curves in Figs. 1(b) and (c), which demonstrate the reflection characteristics of the metasurface at different frequencies. In addition, by introducing asymmetric VO_2 arms, a distinct cross-polarization anomaly is induced at 1.034 THz, as shown in Fig. 1(b). In contrast, when vanadium dioxide is in the metallic state, due to the symmetry of the metallic structure eliminating any chiral properties, the chiral transition at 1.034 THz is eliminated, as depicted in Fig. 1(c). These research findings enable us to utilize the chiral characteristics of the metasurface and the phase transition properties of vanadium dioxide to develop compact integrated metasurface devices.

3 Multifunctional integrated wavefront manipulation

In this section, we propose a multiplexed, multifunctional metasurface capable of flexible manipulation of amplitude and phase, thereby enabling multi-dimensional control over terahertz waves. By varying the geometry, polarization state, and the phase state of VO_2 within each unit structure, it is possible to control the amplitude variation of the meta-atoms. This control extends to the incident frequency, reflected polarization state, and the phase state of VO_2, facilitating multi-dimensional switchable imaging capabilities. The introduction of a geometric phase distribution in the encoding units allows for the demonstration of various polarization multiplexing functions, such as focusing, diverging, and exceptional reflection, across a broad frequency band from 1.0 to 1.2 THz. This integrated, tunable, multifunctional metasurface significantly enhances the efficiency of terahertz wave manipulation and holds considerable promise for applications in high-frequency communication systems.

3.1 Tunable multi-dimensional switchable imaging

Based on the multi-parameter tunable characteristics of the chiral metasurface, we have developed a dynamically tunable multi-dimensional imaging system that utilizes spin-selection. This system is constructed from four chiral metasurface units, each differing in geometric dimensions, as depicted in Fig. 2(a). The reflectance characteristics of these units, under the incidence of

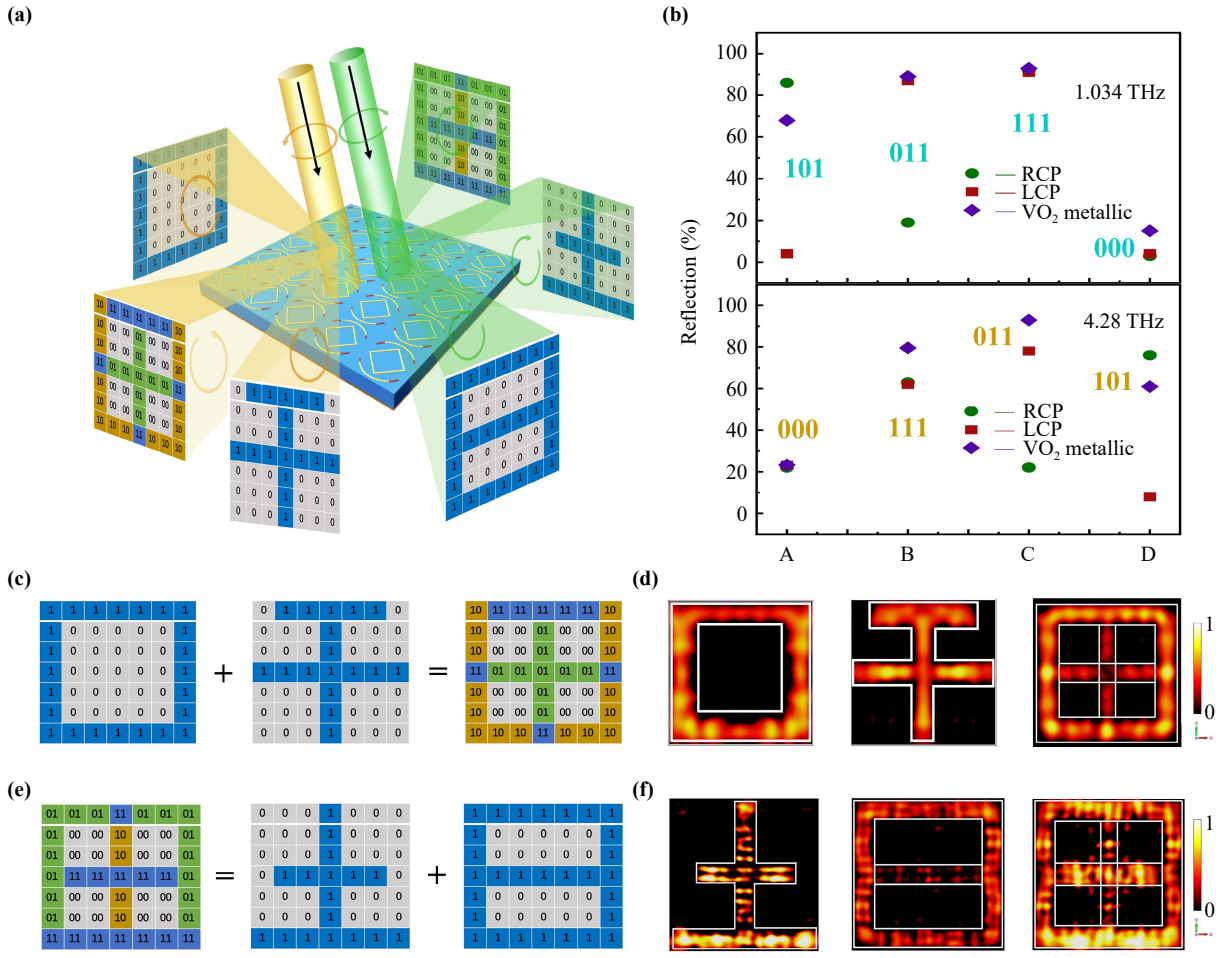

Fig. 2 **(a)** Schematic diagram of switchable imaging. **(b)** Reflectivity of meta-atoms with four different geometric dimensions when vanadium dioxide is in dielectric and metallic states. **(c)** Switchable image design at 1.034 THz. **(d)** Simulated electric field distribution of switchable imaging at frequency 1.034 THz. **(e)** Switchable image design at 4.28 THz. **(f)** Simulated electric field distribution of switchable imaging at frequency 4.28 THz.

LCP and RCP waves, are presented at frequencies of 1.034 THz and 4.28 THz in Fig. 2(b). It is observed that the chiral responses of the units to LCP at 1.034 THz vary significantly. Specifically, the meta-atom A (with dimensions $w_1 = 7$ μm, $w_2 = 11$ μm, $y_1 = 30$ μm, $L_1 = 56$ μm) primarily reflects right-handed circularly polarized light, represented as 10. Conversely, meta-atom B ($w_1 = 6$ μm, $w_2 = 3$ μm, $y_1 = 50$ μm, $L_1 = 56$ μm) reflects predominantly left-handed circularly polarized light, noted as 01. Additionally, meta-atom C ($w_1 = 13$ μm, $w_2 = 8$ μm, $y_1 = 30$ μm, $L_1 = 50$ μm) reflects both left-handed and right-handed circularly polarized components, each exceeding 0.9, and is denoted as 11. Meta-atom D ($w_1 = 14$ μm, $w_2 = 14$ μm, $y_1 = 40$ μm, $L_1 = 45$ μm), however, displays negligible circular polarization in its reflection, represented as 00 due to the removal of its reflective floor.

In the presence of vanadium dioxide in its metallic state, the structural symmetry precludes any chiral properties. This results in nearly identical reflectivities for meta-atoms A, B, C, and D under both LCP and RCP wave irradiation (a detailed analysis is provided in Annex 1). The output polarization components of these meta-atom structures, when analyzed through RCP and LCP analyzers, are encoded as "1" for RCP and "0" for LCP. The amplitude states of vanadium dioxide, whether high or low in its metallic state, are similarly encoded as "1" and "0", respectively. Thus, the four encoded pixels form sequences "000", "011", "101", and "111", as shown in Fig. 2(b). By strategically arranging these four meta-atoms, we achieve a switchable multi-dimensional metasurface image that is controlled by the output polarization state, as illustrated in Fig. 2(a). Each color scale in Fig. 2(c) comprises 3 × 3 units, and the designed image displays traditional Chinese characters. Figure 2(d) details the electric field distribution of the Chinese characters under LCP and RCP wave incidence. The characters "口" and "干" are displayed under RCP and LCP waves, respectively, while the character "田" is manifested when switching vanadium dioxide to

its metallic state. This arrangement demonstrates the feasibility of constructing a display of switchable Chinese characters, controlled via output polarization state, by judiciously configuring meta-atoms with distinct circular polarization conversion properties.

Additionally, it is observed that the polarization state reflected by the chiral metasurface varies with frequency changes. Specifically, at 4.28 THz, the reflectivity of the four meta-atoms is altered, as depicted in Fig. 2(b). At this frequency, when the reflective layer of meta-atom A is removed, it exhibits almost no reflectivity to both LCP and RCP waves, represented as 00. Conversely, the light reflected by meta-atom B contains both left-handed and right-handed circularly polarized components, indicated as 11. Meta-atom C primarily reflects left circularly polarized light, denoted as 01, while meta-atom D primarily reflects right circularly polarized light, represented as 10. When vanadium dioxide is in its metallic state, the structural symmetry eliminates any chiral properties, and the reflectivities of meta-atoms A, B, C, and D to LCP and RCP waves are nearly identical. Upon switching the incident frequency to 4.28 THz, changes in the reflected polarization state of the pixel result in the display of a new Chinese character image, as shown in Fig. 2(e). Figure 2(f) illustrates the electric field distribution for the Chinese characters under the incidence of LCP and RCP terahertz waves. Specifically, the characters "日" and "土" are displayed under LCP and RCP waves, respectively. These characters can be altered to "田" by switching the vanadium dioxide to its metallic state.

The designed MIM metasurface in this work demonstrates significant advantages. This chiral metasurface can obtain four distinct images (the characters "口", "干", "土", and "日") under different CP wave incidences, which together form a complete "田" character information image. In this scenario, if a single channel is compromised, it does not affect the overall information security. Only by decrypting multiple channels simultaneously can the true information be obtained, which greatly enhances information security. Conversely, if data from all four channels are not decrypted at the same time, misleading information will be generated. Therefore, the proposed metasurface can be used for information encryption applications and significantly enhances information security.

3.2 Dynamically tunable polarization multiplexed terahertz beam splitter

In this section, we introduce a method to control polarization multiplexing dynamically using geometric phase manipulation. This is achieved by rotating the upper double split-ring resonators within the chiral metasurface unit, a technique that theoretically supports broadband characteristics [29]. We demonstrate a terahertz polarization multiplexing beam splitter by implementing the necessary geometric phase distribution, as illustrated in Fig. 3(a). When vanadium dioxide is in its dielectric state, the reflection coefficients for the eight units exceed 0.9 under the incidence of RCP and LCP waves. Furthermore, the reflection phases range from –180° to 180° and from 180° to –180° for RCP and LCP waves, respectively, as depicted in Fig. 3(b). It is established that linearly polarized light is essentially a superposition of LCP and RCP light, identical in frequency, amplitude, phase, and propagation direction. Thus, when the beam splitter is exposed to linearly polarized light, the LCP component is focused along the central axis, while the RCP component diverges outward, resulting in effective circular polarization splitting. Figure 3(c) displays the electric field distribution in the x–z and x–y planes at 1.034 THz under LCP incidence, highlighting that the reflected LCP wave is focused at 1145 μm. Conversely, Fig. 3(d) presents the electric field distribution for RCP incidence at the same frequency, showing that the reflected RCP wave diverges at a specific angle.

Upon switching the vanadium dioxide to its metallic state, the upper metal structure is rotated to induce chirality, thereby breaking the symmetry. In this state, the reflection coefficients of the units remain high, above 0.95, for both RCP and LCP incidences, with reflection phases spanning from –180° to 180° and from 180° to –180°, as shown in Fig. 3(e). The electric field distribution at 1.034 THz under LCP incidence, depicted in Fig. 3(f), demonstrates that the reflected LCP wave is now focused at 1267 μm. This represents a shift of 122 μm in focal length compared to when vanadium dioxide is in the dielectric state. Figure 3(g) illustrates the electric field distribution for RCP incidence, indicating that the angle of outward flow is broader when vanadium dioxide is in the dielectric state. Consequently, this terahertz beam splitter can switch polarization multiplexing functions by altering the phase change properties of vanadium dioxide, significantly expanding the potential applications of terahertz beam splitters in multi-channel terahertz communication systems.

The MIM metasurface designed in this work not only satisfies the effect of multi-channel information encryption but also leverages its unique phase modulation capability to achieve broadband and high-efficiency focusing and beam splitting functions on the same platform. By precisely designing the structural parameters of the metasurface, we can achieve efficient beam focusing in the terahertz band, concentrating the optical energy into an extremely small focal region, which is of great significance for high-precision imaging and lithography technologies. In addition, the metasurface also has the capability to split beams, enabling the incident light beam to be precisely divided into multiple directions or multiple wavelengths of light beams, providing a powerful tool for applications such as optical communication and spec-

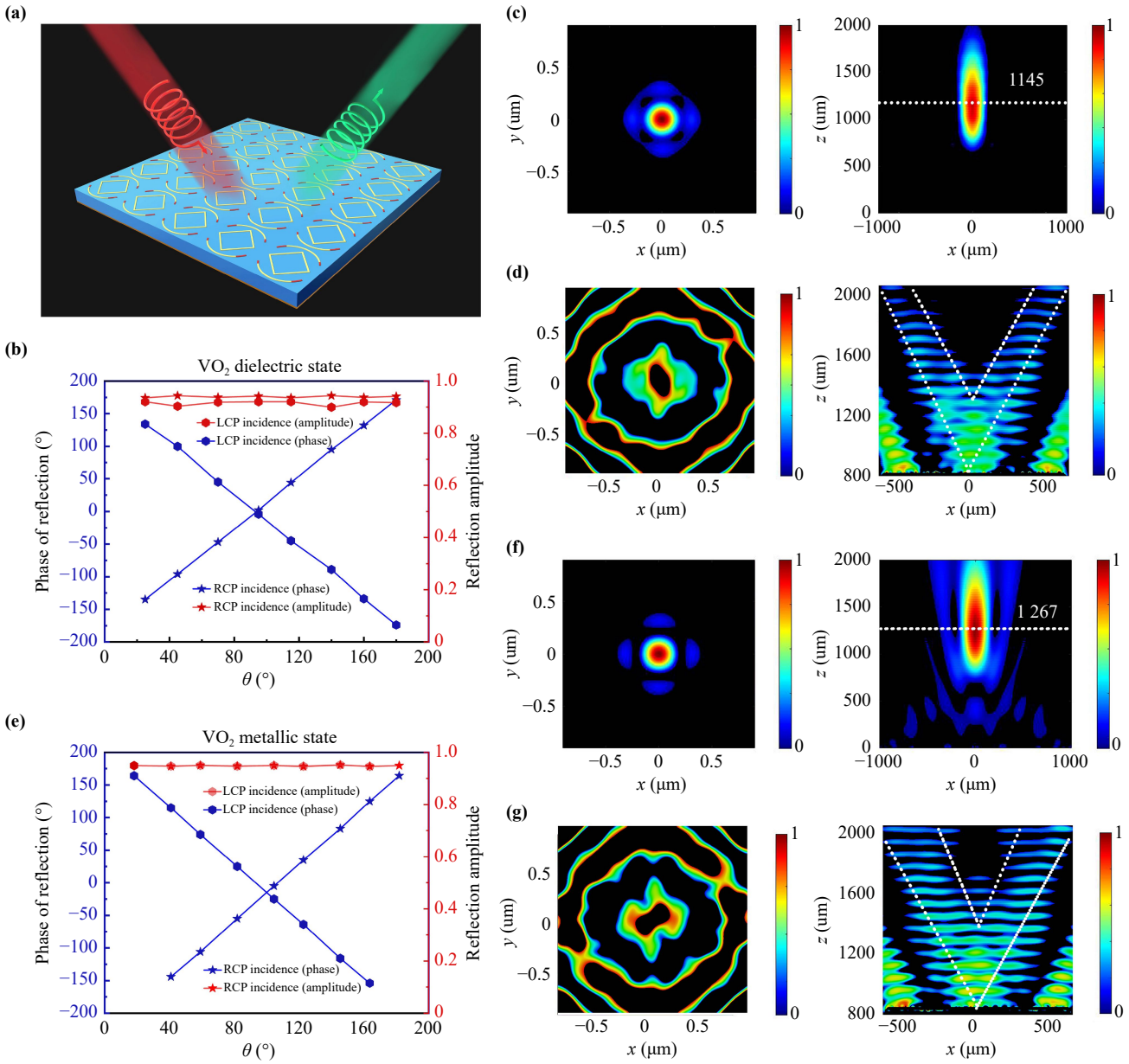

Fig. 3 A circular polarization fractionator controlled by input polarization multiplexing at 1.034 THz. **(a)** Schematic diagrams of the beam splitter under RCP and LCP incidence. **(b)** Polarization reflectivity and geometric phase for eight different rotation angles when vanadium dioxide is in the dielectric state. **(c)** Electric field distribution in the x–y and x–z planes under LCP incidence when vanadium dioxide is in the dielectric state. **(d)** Electric field distribution in the x–y and x–z planes under RCP incidence when vanadium dioxide is in the dielectric state. **(e)** Polarization reflectivity and geometric phase for eight different rotation angles when vanadium dioxide is in the metallic state. **(f)** Electric field distribution in the x–y and x–z planes under LCP incidence when vanadium dioxide is in the metallic state. **(g)** Electric field distribution in the x–y and x–z planes under RCP incidence when vanadium dioxide is in the metallic state.

troscopic analysis. More importantly, the metasurface integrates VO_2 material to achieve dynamic control of the focal length and beam splitter.

3.3 Dynamically tunable polarization multiplexed anomalous reflection device

Building on the eight-unit structure of the terahertz beam splitter depicted in Fig. 3, we further explored the polarization multiplexing anomalous reflection capabilities, as illustrated in Fig. 4. The anomalous reflection metasurface, positioned on the x-plane, comprises eight units that complete a 360° phase cycle arranged in a periodic structure of 2 and subdivided into four groups along the y-axis, resulting in a total configuration of 16 × 16 units. As observed in Figs. 4(a) and (b), when

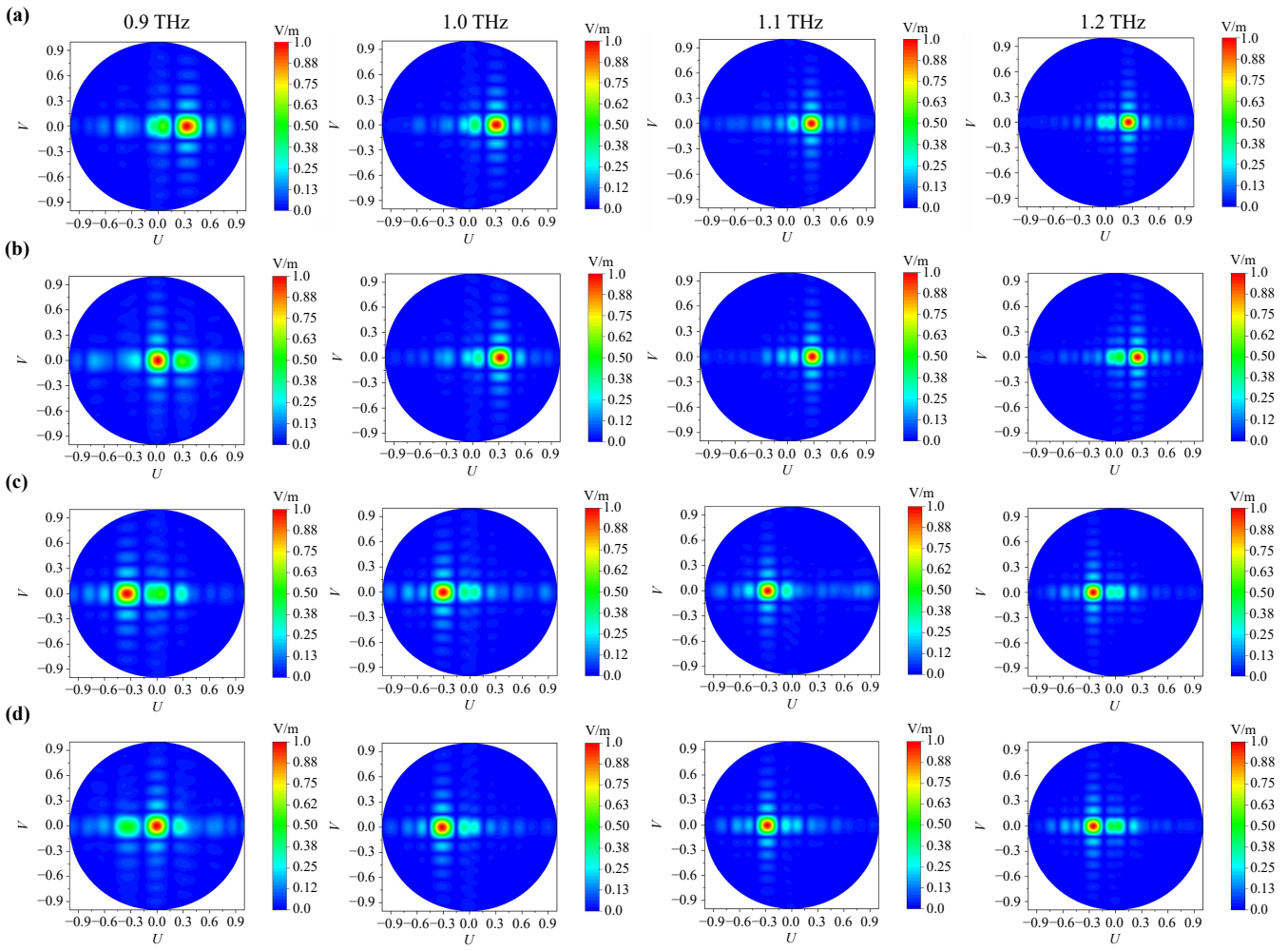

Fig. 4 The abnormal reflection position diagrams obtained at the frequencies of 0.9, 1.0, 1.1, and 1.2 THz, respectively. **(a)** The dielectric state and **(b)** the metal state of the vanadium dioxide under LCP incidence. **(c)** The dielectric state and **(d)** the metal state of the vanadium dioxide under RCP incidence.

vanadium dioxide is in its dielectric state and subjected to LCP waves, the position of its anomalous reflection shifts progressively to the left as the frequency increases from 0.9 to 1.2 THz. Conversely, when vanadium dioxide transitions into its metallic state, the anomalous reflection initially aligns with the central point (0, 0) at 0.9 THz. As the frequency escalates from 1.0 to 1.2 THz, a subsequent movement of the anomalous reflection points gradually resumes towards the left until they once again converge at the center point. Similarly, as depicted in Figs. 4(c) and (d), when vanadium dioxide remains in the dielectric state and encounters RCP waves, the anomalous reflection steadily shifts towards the right as the frequency rises from 0.9 to 1.2 THz. Upon transitioning to the metallic state, the reflection initially positions itself at the center point (0, 0) at 0.9 THz. With a frequency increase from 1.0 to 1.2 THz, the reflection points again commence a gradual drift towards the right until they reach the center for the second time. This observation underscores that the deflection velocity of the anomalous reflection is faster in the metallic state than in the dielectric state. Additionally, by comparing Figs. 4(a) and (c), it is evident that the anomalous reflection positions exhibit a mirror-symmetrical relationship under the influence of LCP and RCP waves, which aligns perfectly with the required chiral characteristic function. This symmetry is consistently observed in Figs. 4(b) and (d) as well. Such dynamically adjustable chiral characteristics hold potential for diverse future applications.

Furthermore, an analysis of the specific positional data of the anomalous reflections at each frequency point, as presented in Fig. 5, reveals that the velocity of vanadium dioxide in its dielectric state is slower compared to its metallic state under both LCP and RCP wave incidences. It is also noted that vanadium dioxide, regardless of whether it is in the dielectric or metallic state, consistently exhibits chirality under the influence of LCP and RCP waves.

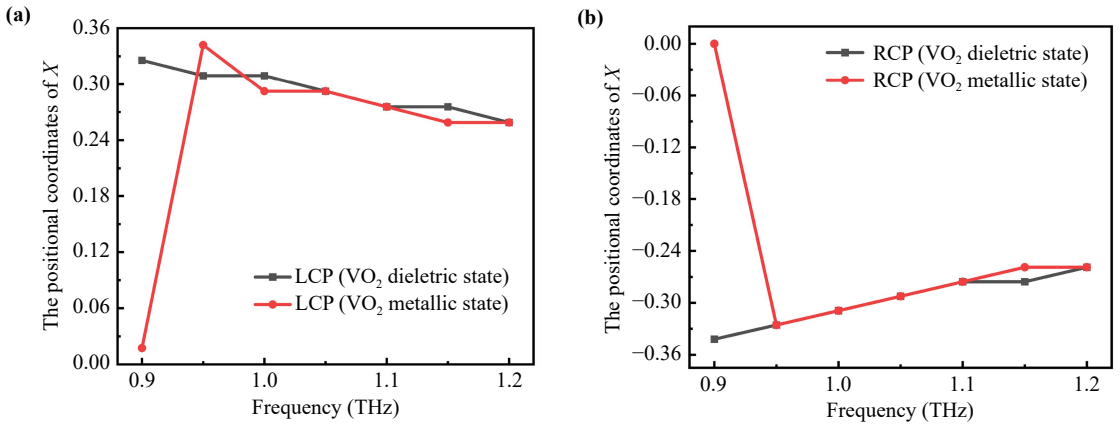

Fig. 5 **(a)** The positional information of abnormal reflections with respect to X when vanadium dioxide is in the dielectric state and the metallic state under the incidence of LCP waves. **(b)** The positional information of abnormal reflections with respect to X when vanadium dioxide is in the dielectric state and the metallic state under the incidence of RCP waves.

4 Conclusion

In this study, we have meticulously designed a chiral metasurface based on a MIM structure. This metasurface not only excels in multi-channel information encryption but also, by ingeniously leveraging the phase characteristics of the metasurface, realizes broadband and high-efficiency focusing and beam splitting functions on the same platform. This multifunctional integration design concept offers a brand-new solution for the efficient control of terahertz waves.

The design of this chiral metasurface skillfully integrates the functions of multi-channel information encryption and optical control. In terms of information encryption, the metasurface can decompose the incident light signal into multiple independent channels, each carrying distinct information, thereby achieving highly secure information transmission and storage. This multi-channel encryption mechanism significantly enhances the confidentiality and anti-interference capability of the information, bringing new possibilities to the fields of modern communication and information security. Simultaneously, by utilizing its unique phase modulation capability, the metasurface achieves broadband and high-efficiency focusing and beam splitting functions on the same platform. By altering the phase transition characteristics of the integrated VO_2 material, dynamic control of the focal length and beam splitter is realized. Therefore, the proposed metasurface holds significant importance for applications in multi-channel optical communication, high-capacity data storage, and optical information encryption, communication, and spectroscopic analysis.

Declarations The authors declare that there are no conflicts of interest related to this article.

Data availability Data underlying the results presented in this paper are not publicly available at this time but may be obtained from the authors upon reasonable request.

Electronic supplementary materials For additional information, please refer to Supplementary Document 1 at https://doi.org/10.15302/frontphys.2025.064203.

Acknowledgements The research has been partially supported by the National Natural Science Foundation of China (No. 62373136), the Fund for State Key Laboratory (No. 6142806230401), the Key Scientific and Technological Project of Science and Technology Department of Henan Province (Nos. 242102211085 and 252102220108), the Guangzhou Basic and Applied Basic Research Project (No. 2025A04J3533), the Zengcheng Economic and Technological Development Zone Science and Technology Innovation Bureau (No. 2024ZCKJ17), the Key Laboratory of Grain Information Processing and Control (Henan University of Technology) of Ministry of Education (No. KFJJ2023002), the Innovative Funds Plan of Henan University of Technology (No. 2022ZKCJ02), and the Open Project of Henan University of Technology Institute for Complexity Science (No. CSKFJJ-2024-32).

References

1. N. Yu and F. Capasso, Flat optics with designer metasurfaces, *Nat. Mater.* 13(2), 139 (2014)
2. W. T. Chen, A. Y. Zhu, and F. Capasso, Flat optics with dispersion-engineered metasurfaces, *Nat. Rev. Mater.* 5(8), 604 (2020)
3. J. P. B. Mueller, N. A. Rubin, R. C. Devlin, B. Groever, and F. Capasso, Metasurface polarization optics: Independent phase control of arbitrary orthogonal states of polarization, *Phys. Rev. Lett.* 118(11), 113901 (2017)
4. W. T. Chen, A. Y. Zhu, J. Sisler, Y. W. Huang, K. M. A. Yousef, E. Lee, C. W. Qiu, and F. Capasso, Broadband achromatic metasurface-refractive optics, *Nano Lett.* 18(12), 7801 (2018)
5. H. Wang, Y. Jing, Y. F. Li, L. Huang, M. Feng, Q. Yuan, J. Wang, J. Zhang, and S. Qu, Spin-selective corner reflector for retro-reflection and absorption by a

circular dichroitic manner, *Photon. Res.* 9(5), 726 (2021)
6. C. Huang, C. Ji, B. Zhao, J. Peng, L. Yuan, and X. Luo, Multifunctional and tunable radar absorber based on graphene-integrated active metasurface, *Adv. Mater. Technol.* 6(4), 2001050 (2021)
7. Z. L. Li, L. G. Deng, J. Deng, Z. He, J. Tao, G. Zheng, and S. Yu, Metasurface-enabled three-in-one nanoprints by multifunctional manipulations of light, *iScience* 24(12), 103510 (2021)
8. Q. B. Fan, M. Z. Liu, C. Zhang, W. Zhu, Y. Wang, P. Lin, F. Yan, L. Chen, H. J. Lezec, Y. Lu, A. Agrawal, and T. Xu, Independent amplitude control of arbitrary orthogonal states of polarization via dielectric metasurfaces, *Phys. Rev. Lett.* 125(26), 267402 (2020)
9. C. L. Zheng, J. Li, Z. Yue, J. Li, J. Liu, G. Wang, S. Wang, Y. Zhang, Y. Zhang, and J. Yao, All-dielectric trifunctional metasurface capable of independent amplitude and phase modulation, *Laser Photonics Rev.* 16(7), 2200051 (2022)
10. Y. J. Bao, F. Nan, J. H. Yan, X. Yang, C. W. Qiu, and B. Li, Observation of full-parameter Jones matrix in bilayer metasurface, *Nat. Commun.* 13(1), 7550 (2022)
11. M. Z. Liu, W. Q. Zhu, P. C. Huo, L. Feng, M. Song, C. Zhang, L. Chen, H. J. Lezec, Y. Lu, A. Agrawal, and T. Xu, Multifunctional metasurfaces enabled by simultaneous and independent control of phase and amplitude for orthogonal polarization states, *Light Sci. Appl.* 10(1), 107 (2021)
12. N. A. Rubin, A. Zaidi, A. H. Dorrah, Z. Shi, and F. Capasso, Jones matrix holography with metasurfaces, *Sci. Adv.* 7(33), eabg7488 (2021)
13. M. Qu, Z. Chen, J. Su, and Z. Li, Design of polarization-reconfigurable beam-scanning monopulse phased array, *IEEE Trans. Antenn. Propag.* 72(3), 2879 (2024)
14. N. K. Grady, J. E. Heyes, D. R. Chowdhury, Y. Zeng, M. T. Reiten, A. K. Azad, A. J. Taylor, D. A. R. Dalvit, and H. T. Chen, Terahertz metamaterials for linear polarization conversion and anomalous refraction, *Science* 340(6138), 1304 (2013)
15. H. Wang, B. F. Zhang, C. Han, and J. Ding, Polarization-multiplexed wavefront-engineering by all-dielectric metasurface with asymmetric polarization-decoupled meta-atoms, *Opt. Express* 29(20), 32377 (2021)
16. Y. Gou, H. F. Ma, Z. X. Wang, L. W. Wu, R. Y. Wu, and T. J. Cui, Dual-band chiral metasurface for independent controls of spin-selective reflections, *Opt. Express* 30(8), 12775 (2022)
17. B. L. Zhang, Z. D. Hu, J. J. Wu, J. Wang, Y. Nie, F. Zhang, M. Li, and S. Khakhomov, Metasurface-based perfect vortex beams with trigonometric-function topological charge for OAM manipulation, *Opt. Lett.* 48(9), 2409 (2023)
18. K. X. Cheng, Z. X. Liu, Z. D. Hu, G. Cao, J. Wu, and J. Wang, Generation of integer and fractional perfect vortex beams using all-dielectric geometrical phase metasurfaces, *Appl. Phys. Lett.* 120(20), 201701 (2022)
19. B. L. Zhang, Z. D. Hu, J. C. Wang, J. Wu, and S. Tian, Creating perfect composite vortex beams with a single all-dielectric geometric metasurface, *Opt. Express* 30(22), 40231 (2022)
20. H. R. Ren, G. Briere, X. Y. Fang, P. Ni, R. Sawant, S. Héron, S. Chenot, S. Vézian, B. Damilano, V. Brändli, S. A. Maier, and P. Genevet, Metasurface orbital angular momentum holography, *Nat. Commun.* 10(1), 2986 (2019)
21. H. R. Ren, X. Y. Fang, J. Jang, J. Bürger, J. Rho, and S. A. Maier, Complex-amplitude metasurface-based orbital angular momentum holography in momentum space, *Nat. Nanotechnol.* 15(11), 948 (2020)
22. H. Y. Zhou, S. Zhang, S. J. Wang, Y. Yao, Q. Cai, J. Lin, X. Zheng, Z. Wang, Z. Tao, Q. He, and L. Zhou, Optically controlled dielectric metasurfaces for dynamic dual-mode modulation on terahertz waves, *Adv. Photonics* 5(2), 026005 (2023)
23. J. Burch, J. Ma, R. I. Hunter, S. A. Schulz, D. A. Robertson, G. M. Smith, J. Wang, and A. Di Falco, Flexible patches for mm-wave holography, *Appl. Phys. Lett.* 115(2), 021104 (2019)
24. R Degl'Innocenti, Terahertz metasurface platform for modulation, holography, and encryption, *Adv. Photonics* 5(2), 020503 (2023)
25. J. Kim, J. Seong, Y. Yang, S. W. Moon, T. Badloe, and J. Rho, Tunable metasurfaces towards versatile metalenses and metaholograms: A review, *Adv. Photonics* 4(2), 024001 (2022)
26. M. Qu, Q. Du, T. Lan, C. Wang, J. Su, and V. Nayyeri, Wideband high-intensity self-bending Bessel-like beam metasurface-based launcher for wireless applications, *IEEE Trans. Microw. Theory Tech.* 72(11), 6349 (2024)
27. H. W. Liang, Q. L. Lin, X. S. Xie, Q. Sun, Y. Wang, L. Zhou, L. Liu, X. Yu, J. Zhou, T. F. Krauss, and J. Li, Ultrahigh numerical aperture metalens at visible wavelengths, *Nano Lett.* 18(7), 4460 (2018)
28. R. Paniagua-Domínguez, Y. F. Yu, E. Khaidarov, S. Choi, V. Leong, R. M. Bakker, X. Liang, Y. H. Fu, V. Valuckas, L. A. Krivitsky, and A. I. Kuznetsov, A metalens with a near-unity numerical aperture, *Nano Lett.* 18(3), 2124 (2018)
29. A. Arbabi, E. Arbabi, M. Mansouree, S. Han, S. M. Kamali, Y. Horie, and A. Faraon, Increasing efficiency of high numerical aperture metasurfaces using the grating averaging technique, *Sci. Rep.* 10(1), 7124 (2020)
30. X. G. Luo, F. Zhang, M. B. Pu, Y. H. Guo, X. Li, and X. L. Ma, Recent advances of wide-angle metalenses: Principle, design, and applications, *Nanophotonics* 11(1), 1 (2021)
31. A. Martins, J. T. Li, B. H. V. Borges, T. F. Krauss, and E. R. Martins, Fundamental limits and design principles of doublet metalenses, *Nanophotonics* 11(6), 1187 (2022)
32. S. Y. Li and C. W. Hsu, Thickness bound for nonlocal wide-field-of-view metalenses, *Light Sci. Appl.* 11(1), 338 (2022)
33. E. Arbabi, J. Q. Li, R. J. Hutchins, S. M. Kamali, A. Arbabi, Y. Horie, P. Van Dorpe, V. Gradinaru, D. A. Wagenaar, and A. Faraon, Two-photon microscopy with a double-wavelength metasurface objective lens, *Nano Lett.* 18(8), 4943 (2018)
34. W. B. Feng, J. C. Zhang, Q. F. Wu, A. Martins, Q. Sun, Z. Liu, Y. Long, E. R. Martins, J. Li, and H. Liang, RGB achromatic metalens doublet for digital

imaging, *Nano Lett.* 22(10), 3969 (2022)
35. S. M. Wang, P. C. Wu, V. C. Su, Y. C. Lai, M. K. Chen, H. Y. Kuo, B. H. Chen, Y. H. Chen, T. T. Huang, J. H. Wang, R. M. Lin, C. H. Kuan, T. Li, Z. Wang, S. Zhu, and D. P. Tsai, A broadband achromatic metalens in the visible, *Nat. Nanotechnol.* 13(3), 227 (2018)
36. W. T. Chen, A. Y. Zhu, V. Sanjeev, M. Khorasaninejad, Z. Shi, E. Lee, and F. Capasso, A broadband achromatic metalens for focusing and imaging in the visible, *Nat. Nanotechnol.* 13(3), 220 (2018)
37. H. P. Zhou, L. Chen, F. Shen, K. Guo, and Z. Guo, Broadband achromatic metalens in the midinfrared range, *Phys. Rev. Appl.* 11(2), 024066 (2019)
38. C. Chen, W. G. Song, J. W. Chen, J. H. Wang, Y. H. Chen, B. Xu, M. K. Chen, H. Li, B. Fang, J. Chen, H. Y. Kuo, S. Wang, D. P. Tsai, S. Zhu, and T. Li, Spectral tomographic imaging with aplanatic metalens, *Light Sci. Appl.* 8(1), 99 (2019)
39. Q. B. Fan, M. Z. Liu, C. Zhang, W. Zhu, Y. Wang, P. Lin, F. Yan, L. Chen, H. J. Lezec, Y. Lu, A. Agrawal, and T. Xu, Independent amplitude control of arbitrary orthogonal states of polarization via dielectric metasurfaces, *Phys. Rev. Lett.* 125(26), 267402 (2020)
40. R. Z. Zhao, B. Sain, Q. S. Wei, C. Tang, X. Li, T. Weiss, L. Huang, Y. Wang, and T. Zentgraf, Multichannel vectorial holographic display and encryption, *Light Sci. Appl.* 7(1), 95 (2018)
41. C. Chen, Y. Q. Wang, M. W. Jiang, J. Wang, J. Guan, B. Zhang, L. Wang, J. Lin, and P. Jin, Parallel polarization illumination with a multifocal axicon metalens for improved polarization imaging, *Nano Lett.* 20(7), 5428 (2020)
42. N. A. Rubin, A. Zaidi, A. H. Dorrah, Z. Shi, and F. Capasso, Jones matrix holography with metasurfaces, *Sci. Adv.* 7(33), eabg7488 (2021)
43. L. Jin, Y. W. Huang, Z. W. Jin, R. C. Devlin, Z. Dong, S. Mei, M. Jiang, W. T. Chen, Z. Wei, H. Liu, J. Teng, A. Danner, X. Li, S. Xiao, S. Zhang, C. Yu, J. K. W. Yang, F. Capasso, and C. W. Qiu, Dielectric multimomentum meta-transformer in the visible, *Nat. Commun.* 10(1), 4789 (2019)
44. H. R. Ren, G. Briere, X. Y. Fang, P. Ni, R. Sawant, S. Héron, S. Chenot, S. Vézian, B. Damilano, V. Brändli, S. A. Maier, and P. Genevet, Metasurface orbital angular momentum holography, *Nat. Commun.* 10(1), 2986 (2019)
45. Y. B. Pan, F. Lan, Y. X. Zhang, H. Zeng, L. Wang, T. Song, G. He, and Z. Yang, Dual-band multifunctional coding metasurface with a mingled anisotropic aperture for polarized manipulation in full space, *Photon. Res.* 10(2), 416 (2022)
46. S. Hu, S. Du, J. Li, and C. Gu, Multidimensional image and beam splitter based on hyperbolic metamaterials, *Nano Lett.* 21(4), 1792 (2021)
47. G. Shang, H. Li, Z. Wang, K. Zhang, S. N. Burokur, J. Liu, Q. Wu, X. Ding, and X. Ding, Coding metasurface holography with polarization-multiplexed functionality, *J. Appl. Phys.* 129(3), 035304 (2021)
48. F. Li, Y. Li, T. Tang, Y. Lu, X. Liu, Y. Liao, and Q. Wen, All-dielectric terahertz metasurface for linearly-polarized multichannel transmission and superposition states of spherical and vortex waves, *Photon. Res.* 11(3), 485 (2023)
49. Y. Y. Yuan, K. Zhang, B. Ratni, Q. Song, X. Ding, Q. Wu, S. N. Burokur, and P. Genevet, Independent phase modulation for quadruplex polarization channels enabled by chirality-assisted geometric-phase metasurfaces, *Nat. Commun.* 11(1), 4186 (2020)
50. C. Q. Jin and Y. M. Yang, Transmissive nonlocal multilayer thin film optical filter for image differentiation, *Nanophotonics* 10(13), 3519 (2021)
51. L. Lu, C. H. Bu, Z. L. Su, B. Guan, Q. Yu, W. Pan, and Q. Zhang, Generative deep-learning-embedded asynchronous structured light for three-dimensional imaging, *Adv. Photonics* 6(4), 46004 (2024)
52. H. Zhao, X. Wang, S. Liu, and Y. Zhang, Highly efficient vectorial field manipulation using a transmitted tri-layer metasurface in the terahertz band, *Opto-Electronic Adv.* 6(2), 220012 (2023)
53. F. Fan, W. H. Gu, S. Chen, X. H. Wang, and S. J. Chang, State conversion based on terahertz plasmonics with vanadiμm dioxide coating controlled by optical pμmping, *Opt. Lett.* 38(9), 1582 (2013)
54. Y. Zhao, Q. P. Huang, H. L. Cai, X. Lin, and Y. Lu, A broadband and switchable VO_2-based perfect absorber at the THz frequency, *Opt. Commun.* 426(1), 443 (2018)
55. C. Chen, S. L. Gao, W. G. Song, H. Li, S. N. Zhu, and T. Li, Metasurfaces with planar chiral meta-atoms for spin light manipulation, *Nano Lett.* 21(4), 1815 (2021)
56. P. Gao, C. Chen, Y. W. Dai, X. Wang, H. Cui, X. Zhu, and H. Liu, Reconfigurable Janus metasurface with chiral meta-atoms for multi-channel vortex beams and holography multiplexing, *Opt. Express* 33(1), 309 (2025)
57. C. Song, X. P. Zhang, F. Y. Ma, Y. Yin, H. Yin, S. Wang, and L. Zhao, Design and evaluation of wheat moisture content detection device based on a stripline, *Agriculture* 14(3), 471 (2024)
58. H. Xu, W. S. Zhao, W. J. Wu, D. W. Wang, H. Gao, Y. Hu, and J. Liu, Miniaturized microwave microfluidic sensor based on quarter-mode 2.5-D spoof plasmons, *Sens. Actuators A Phys.* 342(1), 113621 (2022)
59. Z. Liao, X. Peng, L. L. Liu, Y. Xu, K. D. Xu, B. Pan, G. Q. Luo, and Y. Liu, Microwave plasmonic exceptional points for enhanced sensing, *Laser Photonics Rev.* 17(11), 2300276 (2023)
60. H. Y. Jeong, Y. Lim, J. Han, S. C. An, and Y. C. Jun, Electrical addressing of exceptional points in compact plasmonic structures, *Nanophotonics* 12(11), 2029 (2023)
61. M. Gao, X. Wang, S. Luo, Q. Lu, S. N. Luo, C. Lu, S. Chen, F. Long, and Y. Lin, Terahertz transmission properties of vanadium dioxide films deposited on gold grating structure with different periods, *Mater. Res. Express* 7(5), 056404 (2020)
62. A. Krasnok, M. Tymchenko, and A. Alù, Nonlinear metasurfaces: A paradigm shift in nonlinear optics, *Mater. Today* 21(1), 8 (2018)